

Código seguro de Verificación: GEN-5b4e-e946-617b-c6b0-3d9f-f9e9-eee5-61f3 | Puede verificar la integridad de este documento en la siguiente dirección:
<https://sara.ciemat.es:8443/csv/CsvRecoverService?csv=5b4ee946617bc6b03d9ff...>

**PRODUCTION AND CHARACTERIZATION OF Cr-DOPED UO₂ AS AN ATF
SURROGATE BY DRY POWDER METHOD
(IONMAT PROJECT. SUBTASK 2.1)**

DIVISIÓN DE FISIÓN NUCLEAR



Centro de Investigaciones
Energéticas, Medioambientales
y Tecnológicas

CSV : GEN-5b4e-e946-617b-c6b0-3d9f-f9e9-eee5-61f3

DIRECCIÓN DE VALIDACIÓN : <https://sara.ciemat.es:8443/csv/CsvRecoverService?csv=5b4ee946617bc6b03d9ff...>

FIRMANTE(1) : M.SOLEDAD FERNANDEZ FERNANDEZ | FECHA : 28/05/2024 12:37 | Sin acción específica

FIRMANTE(2) : MARIA NIEVES RODRIGUEZ VILLAGRA | FECHA : 28/05/2024 12:38 | Sin acción específica

FIRMANTE(3) : SERGIO FERNANDEZ CARRETERO | FECHA : 28/05/2024 12:39 | Sin acción específica



Ciemat DIVISIÓN DE FISIÓN NUCLEAR	INFORME DFN/RA-03/SP-24	HOJA 1 DE 38
	REF. EXTERNA	REVISIÓN 0

TITULO: Production and characterization of Cr-doped UO₂ as an ATF surrogate by dry powder method (IONMAT project. Subtask 2.1)

AUTORES: N. Rodríguez-Villagra, A. Milena-Pérez, S. Fernández-Carretero, L.J. Bonales, L. Gutiérrez, A., Núñez, L. Serrano, S. Durán, L. Anta, J. Cobos, H. Galán

ABSTRACT:

The accident at the Fukushima Daiichi NPP has revealed the need for improved safety margins of current nuclear energy, which can be attained by the development of Advanced Tolerant Fuel (ATF). This fact, together with the demand for an improved fuel performance in the reactor, results in an increased fuel burnup as well as improving its resistance to alteration performance during and after irradiation. The development of manufacturing processes to produce of ATFs is of utmost importance. To a good extent, the relevance of experimental observations depends on a suitable representation of those fuels. Based on terms of safety, economy, and compatibility, in this task, the effects of different fabrication method both via powder metallurgical routes and co-precipitation route (followed by calcination and sintering) on the grain growth of UO₂ will be systematically studied. Here fabrication via dry route is presented. The materials proposed for this work are pure UO₂ and doped UO₂ and will try to mimic the manufacture of ATF. The Cr as Cr₂O₃ is used as dopant in ATF to reinforce the integrity of the UO₂ in operation during its irradiation. The aim of additives in UO₂ fuel is to increase the fuel resistance by means of an enlargement of the average grain size on the matrix (densification) and the plasticity of the fuel in present LWRs. This change in grain size alters the diffusion phenomena of Fission Product (FP) inside the fuel pellets, causing an increased retention of the gaseous products inside the ceramic matrix.

	NOMBRE	FIRMA	FECHA	FECHA DE EMISIÓN
Preparado por:	N. Rodríguez-Villagra			
Revisado por:	S. Fernández-Carretero			
Conf por A. C.:	S. Fernández			
Aprobado por:	E.M. González			



Ciemat DIVISIÓN DE FISIÓN NUCLEAR	INFORME DFN/RA-03/SP-24	HOJA 2 DE 38
	REF. EXTERNA	REVISIÓN 0 FECHA 12/04/2024

INDEX

1.	INTRODUCTION.....	6
2.	EXPERIMENTAL PROCEDURE. EQUIPMENT AND EXPERIMENTAL TECHNIQUES.....	9
2.1.	EFFECT OF SINTERING CONDITIONS: SAMPLE PREPARATION AND THERMAL CONDITIONS.....	9
2.2.	EFFECT OF DOPANT CONTENT. MATERIALS: SAMPLE PREPARATION AND CHARACTERIZATION.....	14
3.	RESULTS.....	15
3.1.	EFFECT OF SINTERING CONDITIONS	15
3.2.	EFFECT OF DOPANT CONTENT.....	18
3.2.1.	SEM: grain size and segregated phases.....	18
3.2.2.	XRD	20
3.2.3.	Raman spectroscopy and fluorescence spectral analysis.....	23
3.2.3.1.	Fluorescence.....	24
3.2.3.2.	Raman Intensity.....	25
3.2.3.3.	Profile Analysis of the LO Band	26
4.	CONCLUSIONS	31
5.	ACKNOWLEDGEMENTS	33
6.	REFERENCES	34

Código seguro de Verificación: GEN-5b4e-e946-617b-c6b0-3d9f-f9e9-eee5-61f3 | Puede verificar la integridad de este documento en la siguiente dirección:
<https://sara.ciemat.es:8443/csv/CsvRecoverService?csv=5b4ee946617bc6b03d9ff9e9eee561f3...>

CSV : GEN-5b4e-e946-617b-c6b0-3d9f-f9e9-eee5-61f3

DIRECCIÓN DE VALIDACIÓN : <https://sara.ciemat.es:8443/csv/CsvRecoverService?csv=5b4ee946617bc6b03d9ff9e9eee561f3>

FIRMANTE(1) : M.SOLEDAD FERNANDEZ FERNANDEZ | FECHA : 28/05/2024 12:37 | Sin acción específica

FIRMANTE(2) : MARIA NIEVES RODRIGUEZ VILLAGRA | FECHA : 28/05/2024 12:38 | Sin acción específica

FIRMANTE(3) : SERGIO FERNANDEZ CARRETERO | FECHA : 28/05/2024 12:39 | Sin acción específica



Ciemat DIVISIÓN DE FISIÓN NUCLEAR	INFORME DFN/RA-03/SP-24	HOJA 3 DE 38
	REF. EXTERNA	REVISIÓN 0 FECHA 12/04/2024

INDEX OF FIGURES

Figure 1 Thermal treatment cycle (temperature, ramp and atmosphere) applied to obtain the UO ₂ powder.....	10
Figure 2 Raman spectra of UO ₂ (left) and Cr ₂ O ₃ (right) and 2 nd derivative curves. Labels a) to j) correspond to the Raman modes found in the spectra, assigned in Table III.	11
Figure 3 XRD patterns of starting Cr ₂ O ₃ (left) and UO ₂ (right), together with their respective ICDD reference data.	12
Figure 4 SEM images of starting powders of a) UO ₂ and b) Cr ₂ O ₃	12
Figure 5 Fabrication flow diagram of conventional “dry route” used in CIEMAT for pellet production.....	13
Figure 6 Diffraction patterns of doped UO ₂ pellets with 600 ppm of Cr ₂ O ₃ at different sintering conditions. See correspondence to labels in Table IV.....	15
Figure 7 Raman spectra of doped UO ₂ pellets with 600 ppm of Cr ₂ O ₃ at different sintering conditions. See correspondence to labels in Table IV.	16
Figure 8 Grain size and SEM images (A) and density values (B). See correspondence to labels in ¡Error! No se encuentra el origen de la referencia.....	16
Figure 9 Adsorption isotherms (solid lines) and desorption isotherms (dashed lines) (A), BET surface area (B), and porosity analysis (C).....	17
Figure 10 Representative SEM images of the analyzed pellets: a) pure UO ₂ , b) UO ₂ _200Cr ₂ O ₃ , c) UO ₂ _600Cr ₂ O ₃ , d) UO ₂ _1000Cr ₂ O ₃ , e) UO ₂ _6000Cr ₂ O ₃	18
Figure 11 Average grain size of the studied disks vs Cr ₂ O ₃ content. Uncertainty bands correspond to the repeatability of the measurements.	19
Figure 12 Back scattered SEM images of chromium precipitates in a grain boundaries in samples doped with a) 1000 ppm and b) 6000 ppm of Cr ₂ O ₃ , respectively.....	20
Figure 13 a) Diffraction patterns of the studied samples and b) the (531) Kα1,2 doublet at 113° of the normalized diffraction patterns.....	21
Figure 14 Lattice parameter vs Cr ₂ O ₃ concentration and graphical calculation of solubility limit of Cr ₂ O ₃ in the UO ₂ matrix for the samples studied. Uncertainty bands correspond to the repeatability of the measurements.	22
Figure 15 Lattice parameter vs average grain size of the analysed pellets. Black squares correspond to samples with Cr ₂ O ₃ content lower than the solubility limit, while the open triangle represents the pellet doped with 6000 ppm of Cr ₂ O ₃ , which is higher than the solubility limit. Uncertainty bands correspond to the repeatability of the measurements.	23
Figure 16 Raman spectra of chromia-doped UO ₂ pellets.....	24
Figure 17 Number of spectrums showing Cr ³⁺ -fluorescence peaks (per 10 spectrums acquired for each simple).....	25
Figure 18 Area evolution of the T _{2g} (445 cm ⁻¹) and 2LO (1140 cm ⁻¹) bands with Cr ₂ O ₃ concentration. Solid symbols correspond to samples with Cr ₂ O ₃ content lower than the solubility limit,	



Ciemat DIVISIÓN DE FISIÓN NUCLEAR	INFORME DFN/RA-03/SP-24	HOJA 4 DE 38
	REF. EXTERNA	REVISIÓN 0 FECHA 12/04/2024

while open triangles represent the pellet doped with 6000 ppm of Cr₂O₃, which is higher than the solubility limit. Dashed line represents a guide to the eye to show the general trend of data. Uncertainty bands correspond to the repeatability of the measurements.....26

Figure 19 Raman spectra of a UO₂ disk doped with a) 600 ppm and b) 1000ppm of Cr₂O₃ by Lorentzian peaks at 445, 545 and 570 cm⁻¹.....27

Figure 20 Evolution of the intensity of the peaks at 570 cm⁻¹ (LO band, black squares) and 545 cm⁻¹ (red circles), both referred to the T_{2g} band, with the Cr₂O₃ content. Solid symbols correspond to samples with Cr₂O₃ content lower than the solubility limit, while open triangles represent the pellet doped with 6000 ppm of Cr₂O₃, which is higher than the solubility limit. Dashed line represents a guide to the eye to show the general trend of data. Uncertainty bands correspond to the repeatability of the measurements.28

Figure 21 LO band area ratio vs grain size of the analysed pellets. Black squares correspond to samples with Cr₂O₃ content lower than the solubility limit, while the open triangle represents the pellet doped with 6000 ppm of Cr₂O₃, which is higher than the solubility limit. Uncertainty bands correspond to the repeatability of the measurements.29

Figure 22 Lattice parameter *vs* A_{LO}/A_{T_{2g}} peaks ratio. Black squares correspond to samples with Cr₂O₃ content lower than the solubility limit, while the open triangle represents the pellet doped with 6000 ppm of Cr₂O₃, which is higher than the solubility limit. Uncertainty bands correspond to the repeatability of the measurement.....30



Ciemat DIVISIÓN DE FISIÓN NUCLEAR	INFORME DFN/RA-03/SP-24	HOJA 5 DE 38
	REF. EXTERNA	REVISIÓN 0 FECHA 12/04/2024

INDEX OF TABLES

Table I Methods and techniques used in this project.	9
Table II Raw material characterization.	10
Table III Raman modes of starting powders used in this work.	11
Table IV Heating stages and sintering time, include label for each system. UO ₂ doped with 600 ppm Cr ₂ O ₃	13
Table V Definition of samples.	14

Código seguro de Verificación: GEN-5b4e-e946-617b-c6b0-3d9f-f9e9-eee5-61f3 | Puede verificar la integridad de este documento en la siguiente dirección:
<https://sara.ciemat.es:8443/csv/CsvRecoverService?csv=5b4ee946617bc6b03d9ff9e9eee561f3...>

CSV : GEN-5b4e-e946-617b-c6b0-3d9f-f9e9-eee5-61f3

DIRECCIÓN DE VALIDACIÓN : <https://sara.ciemat.es:8443/csv/CsvRecoverService?csv=5b4ee946617bc6b03d9ff9e9eee561f3>

FIRMANTE(1) : M.SOLEDAD FERNANDEZ FERNANDEZ | FECHA : 28/05/2024 12:37 | Sin acción específica

FIRMANTE(2) : MARIA NIEVES RODRIGUEZ VILLAGRA | FECHA : 28/05/2024 12:38 | Sin acción específica

FIRMANTE(3) : SERGIO FERNANDEZ CARRETERO | FECHA : 28/05/2024 12:39 | Sin acción específica



Ciemat DIVISIÓN DE FISIÓN NUCLEAR	INFORME DFN/RA-03/SP-24	HOJA 6 DE 38
	REF. EXTERNA	REVISIÓN 0 FECHA 12/04/2024

1. INTRODUCTION

In recent years, Accident Tolerant Fuels (ATF) types for operating Light Water Reactors (LWR) have been developed, with the aim of extending power output (burn-up) in UO₂-based fuels, controlling in operating nuclear reactors and enhancing the accident tolerance in commercial nuclear power plants [1-4]. Current Light Water Reactors (LWR) are typically designed to achieve a burn-up about 50 GWd/tU, but with newer fuel technology (*i.e.* doped fuels), these same LWRs are now capable of achieving up to 60 or even 70 GWd/tU with the present enrichment limit (between 3-5% ²³⁵U) [5-7]. However, several processes need to be taken into consideration at high burn-up. Especially important are the Fission Gas Release (FGR) and the Pellet-Cladding Interaction (PCI), which decreases the flexibility of the reactor, *i.e.*, reduces the capability of the reactor to extend the burn-up in the established security requirements [8]. Both processes could compromise the safety margins in nuclear power plants, and needs to be minimized. In the attempt to optimize reactor operation and increase energy production efficiency, the nuclear energy industry is continuously developing new types of fuels.

The use of mixed oxide (MOX) fuel has become frequent in the past years, as well as Gd₂O₃-doped UO₂ [9, 10]. More recently, improved fuels referred as ATF [11] are made by the refinement of the fuel microstructure by using different dopants and clad designs. The purpose of these additives is to increase the fuel resistance by means of an enlargement of the average grain size of the matrix (densification) and the plasticity of the fuel in traditional LWRs. It is known that this change in grain size alters the diffusion phenomena of FP inside the fuel pellets, causing an increased retention of the gaseous products inside the ceramic matrix [12]. In order to address this issue, different dopants have been considered through the years, including oxides of chromium [8, 13-16], magnesium [14, 17], niobium [18] or titanium [19], among others. In addition, several investigations have been carried out studying the performance of some of these dopants together, *e.g.* aluminosilicates [20].

The addition of Cr₂O₃ and (Cr₂O₃+Al₂O₃) to UO₂ fuel matrix has been considered to modulate the microstructure triggering grain growth during sintering of the UO₂ pellets and minimizing the FGR [21, 22]. This will essentially lower the PCI inside the fuel rods, allowing higher “burnups” than traditional UO₂ fuel. While doped fuels imply an in-reactor performance improvement (in the sense of safety, competitiveness, and economics) [23], it



Ciemat DIVISIÓN DE FISIÓN NUCLEAR	INFORME DFN/RA-03/SP-24	HOJA 7 DE 38
	REF. EXTERNA	REVISIÓN 0 FECHA 12/04/2024

is not known whether the degradation behavior of such fuels in the back-end environment compared to standard fuel. Specifically, chromia (Cr_2O_3) doped fuel has turned out to be an especially effective alternative to traditional UO_2 fuel (today used in LWRs) in the grain growth process during sintering, also showing a great improvement on PCI and fission gas retention [8, 16, 24, 25]. In fact, adding an amount of chromia close to the solubility limit has demonstrated to improve this behavior [16]. The design of the ATF concepts are included in the strategic agenda of CEIDEN platform and SNETP initiative [26] because on an improved economics and safety margins of nuclear fuels.

This document presents the results from task 2 “*Fabrication of Advanced Tolerant Fuel pellets and degradation studies*”, specifically those coming from subtask 2.1 “*Production and characterization of ATF by dry powder method*” within the framework of the PID2021-124913OA-I00 project (IONMAT project) funded by the Spanish State Research Agency (*Agencia Española de Investigación*, AEI) [27]. The broad goal of this project is to evaluate potential ways of obtaining nuclear fuels, simulated irradiated fuels (not irradiated) and doped matrices. Overall, task 2 focuses on studying the influence of fabrication methods and parameters (powder, mixing technology, sintering atmosphere, pressure, additive content) on the grain growth of UO_2 for Cr doped- UO_2 pellets. The materials planned for this work will mimic the manufacture of ATF (Cr- UO_2 doped to reinforce the integrity of the UO_2 in operation during its irradiation). The precise knowledge of the influence of synthesis parameters, for instance, the thermal treatment of precursors, method and amount of chromium doping, during the sintering of the pellets facilitates the commercial production of materials with a hand tailored microstructure with respect to the density, grain size, and chromium grain distribution. Within subtask 2.1, the influence of the above mentioned fabrication parameters and Cr content on the grain size of UO_2 by dry powder method is studied under different sintering conditions. The methodology applied consists on classic powder metallurgy system. It is done by means of grinding / sieving, pressing green pellets and after calcining and sintering at high temperature and under controlled atmosphere conditions. The materials proposed for this subtask are Cr-doped UO_2 pellets with different Cr_2O_3 contents (from 0 to 6000 ppm).

The specific objectives of subtask 2.1 are:

1. Effect of sintering conditions:



Ciemat DIVISIÓN DE FISIÓN NUCLEAR	INFORME DFN/RA-03/SP-24	HOJA 8 DE 38
	REF. EXTERNA	REVISIÓN 0 FECHA 12/04/2024

- Sintering atmosphere: reducing (4.7% H₂/N₂).
- Sintering temperature/time: 1000-1700°C for 1-10 h.
- Pressing pressures (uniaxial): 700 MPa

2. Effect of dopant content (Cr₂O₃): 0 – 6000 ppm.

Código seguro de Verificación: GEN-5b4e-e946-617b-c6b0-3d9f-f9e9-eee5-61f3 | Puede verificar la integridad de este documento en la siguiente dirección:
<https://sara.ciemat.es:8443/csv/CsvRecoverService?csv=5b4ee946617bc6b03d9ff9e9eee561f3ff...>

CSV : GEN-5b4e-e946-617b-c6b0-3d9f-f9e9-eee5-61f3

DIRECCIÓN DE VALIDACIÓN : <https://sara.ciemat.es:8443/csv/CsvRecoverService?csv=5b4ee946617bc6b03d9ff9e9eee561f3>

FIRMANTE(1) : M.SOLEDAD FERNANDEZ FERNANDEZ | FECHA : 28/05/2024 12:37 | Sin acción específica

FIRMANTE(2) : MARIA NIEVES RODRIGUEZ VILLAGRA | FECHA : 28/05/2024 12:38 | Sin acción específica

FIRMANTE(3) : SERGIO FERNANDEZ CARRETERO | FECHA : 28/05/2024 12:39 | Sin acción específica



Ciemat DIVISIÓN DE FISIÓN NUCLEAR	INFORME DFN/RA-03/SP-24	HOJA 9 DE 38
	REF. EXTERNA	REVISIÓN 0 FECHA 12/04/2024

2. EXPERIMENTAL PROCEDURE, EQUIPMENT AND EXPERIMENTAL TECHNIQUES

For the accomplishment of the objectives, the listed methods/techniques (see Table I) were used.

Technique	Parameter	Equipment
BET	N ₂ -BET Surface Area V abs(N ₂ , cm ₃ /g) vs P/P ₀	ASAP 2020 (Micromeritics) ISO 12800E
XRD	Microstructure/crystalline identification Intensity vs diffraction angle Lattice parameters Quantification of phase mixtures	D8 ADVANCE Eco (Bruker) – ICDD Cu K α radiation ($\lambda=1.54056\text{ \AA}$), 40 kV and 25 mA Bragg-Brentano configuration geometry software TOPAS (Bruker Analytical X-Ray Systems)
Raman spectroscopy	Structural / speciation Characteristic spectrum (“fingerprint”) by changing molecular bonds with light (laser): intensity vs frequency ($\Delta\nu$ incident-scattered)	LabRam HR Evolution (HORIBA) He-Ne laser with wavelength=632.8 nm.
SEM-EDX	Surface morphology/grain size/Elemental identification (quantification) Lineal intercept method (Heyn) Scattered electrons from the surface. (I vs ev)	TM4000 Plus 15 kV (HITACHI) ASTM E 112-96 ;UNE-EN ISO 643:2012
Laser diffraction	Particle size distribution	Malvern, Series 2600 Malvern Mastersizer 3000 Hydro EV and Aero S
Archimedean method	Density	Sartorius kit
Furnace	1700°C, atmosphere	Termolab
Polisher		Vector LC250 (Buehler)
Mixer Mill	Max. frequency of 30 Hz	MM 400 (Retsch)
Uniaxial Press	25 T	C256C (Power team, Johannesburg, South Africa)

Table I Methods and techniques used in this project.

2.1. EFFECT OF SINTERING CONDITIONS: SAMPLE PREPARATION AND THERMAL CONDITIONS

For the objective 1 (see section 1), the UO₂ was obtained via Ammonium Di-Uranate (ADU) following a precipitation process that involves several major steps. First of all, UO₂ is dissolved in highly concentrated HNO₃, followed by filtration of the resultant solution to eliminate possible solid impurities. After that, purification of uranium is carried out by



Ciemat DIVISIÓN DE FISIÓN NUCLEAR	INFORME DFN/RA-03/SP-24	HOJA 10 DE 38
	REF. EXTERNA	REVISIÓN 0 FECHA 12/04/2024

applying a selective solvent extraction process with tributyl phosphate (TBP), a compound widely used on an industrial scale [28, 29]. Once a pure uranium solution was obtained, it was precipitated by using NH₄OH (30 %). The precipitated powder was then separated by using HA 0.45 µm (Millipore) filters, and identified as ADU [30, 31]. Finally, this powder was subjected to a thermal treatment for denitration/dehydrating, calcine and reduce it to its final form of UO₂. The conditions of such a treatment are presented in the flowchart of Figure 1. The Cr₂O₃ powders were provided by Alfa Aesar.

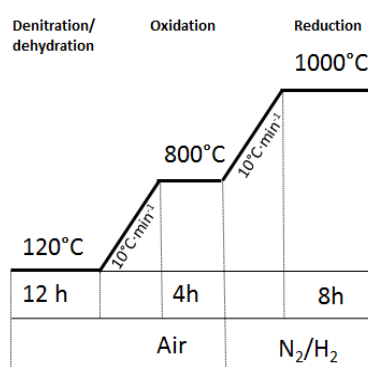


Figure 1 Thermal treatment cycle (temperature, ramp and atmosphere) applied to obtain the UO₂ powder.

Prior to the sintering of the samples, raw powders have been characterized in terms of the Specific Surface Area (SSA) by BET with N₂ and the mean particle size by Laser Diffraction. The results of this characterization can be seen in Table II¹.

Material	SSA (BET) (m ² ·g ⁻¹)	Average particle size (µm)
UO ₂	0.95±0.02	15.23±0.57
Cr ₂ O ₃	3.47±0.02	2.09±0.34

Table II Raw material characterization.

¹ The average particle size presented in **¡Error! No se encuentra el origen de la referencia.** refers to the average diameter of a discrete solid material, in this case a powder, and it is not related with the grain size, which refers to the average diameter of the individual crystal orientations located in poly-crystalline materials, and measured by SEM and presented further on for sintered pellets.



Starting powders also have been measured by Raman spectroscopy, XRD and SEM. Raman spectrum of UO₂ powder (Figure 2 at left) shows the well-known features of uranium dioxide: a) the triply degenerate T_{2g} mode at 445 cm⁻¹, b) the almost indistinguishable LO mode at about 570 cm⁻¹, and c) the first overtone of the LO mode (2LO) centered about 1140 cm⁻¹ [32-34]. These bands are summarized in Table III (a-c). In addition, Cr₂O₃ spectrum (Figure 2 at right) shows the classic bands and features described in the literature [35-38]. The corresponding Raman shifts of both materials are shown in Table III (d-j), together with the Raman modes that represent. In both cases, spectra shown in Figure 2 are the sum of 10 spectra of each powder.

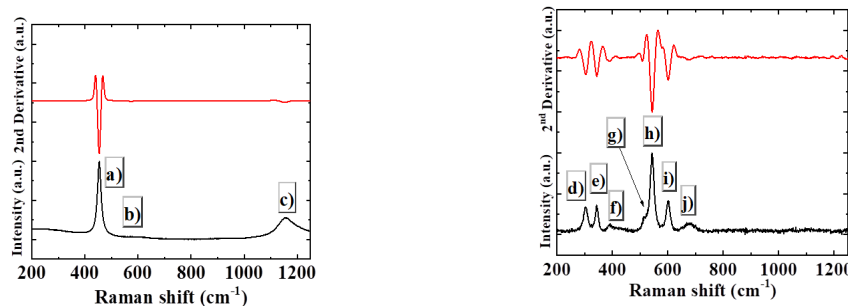


Figure 2 Raman spectra of UO₂ (left) and Cr₂O₃ (right) and 2nd derivative curves. Labels a) to j) correspond to the Raman modes found in the spectra, assigned in Table III.

Experimental Raman shifts for UO ₂ (± 1 cm ⁻¹)	Raman shifts for UO ₂ (cm ⁻¹) by other authors[33, 34]	Raman mode assigned (UO ₂) [33, 34]
a) 445	445 [33, 34]	T _{2g} [33, 34]
b) 570	575 [33]	LO phonon [34]
c) 1140	1150 [33, 34]	2LO phonon overtone [33, 34]
Experimental Raman shifts for Cr ₂ O ₃ (± 1 cm ⁻¹)	Raman shifts for Cr ₂ O ₃ (cm ⁻¹) by other authors [35, 36, 38]	Raman mode assigned (Cr ₂ O ₃) [35, 36, 38]
d) 303	303 [38]	A _{1g} [38]
e) 344	348 [38]	Eg [38]
f) 390	397 [38]	Eg [38]
g) 524	530 [38]	Eg [38]
h) 543	547 [38]	A _{1g} [38]
i) 601	609 [38]	Eg [38]
j) 680	691 [35, 36]	CrO ₂ [35, 36]

Table III Raman modes of starting powders used in this work.



Starting powders have been characterized, in terms of their XRD patterns, and compared with the standards, retrieved from ICDD references 03-065-0285 (UO_2) and 00-006-0504 (Cr_2O_3), in order to confirm the purity of the materials. The results can be seen in Figure 3.

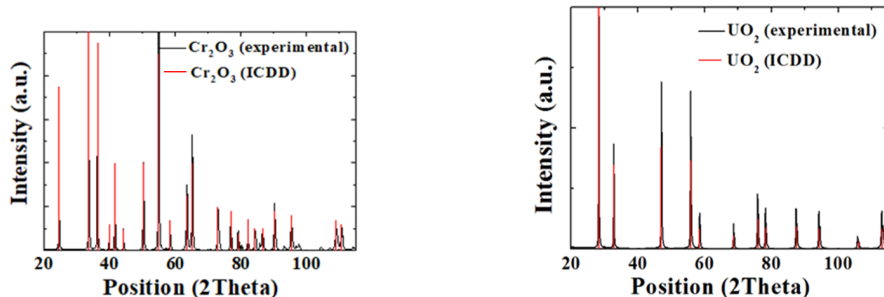


Figure 3 XRD patterns of starting Cr_2O_3 (left) and UO_2 (right), together with their respective ICDD reference data.

Finally, SEM images have been also acquired from each starting powder. A representative example of each one is shown in Figure 4. In both cases, SEM observations reveal that the powder morphology consists of blunt and round particles, similar to microspheres. This shape is appropriated in the sintering of the pellets [39]. It is also remarkable the fact that particle size of Cr_2O_3 is smaller than UO_2 , as presented in Table II and seen in Figure 4.

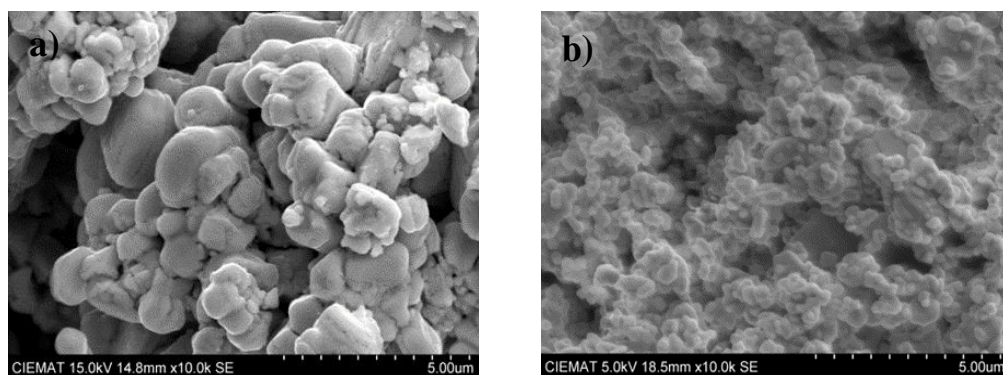


Figure 4 SEM images of starting powders of a) UO_2 and b) Cr_2O_3 .

Next, both materials (purified UO_2 and Cr_2O_3) were homogenized together with the binder in a mill-homogenizer at 15 Hz for 15 minutes. Then, following a conventional metallurgical procedure, the mixtures obtained were subjected to uniaxial pressing with an applied pressure of 700 MPa. After that, a heating process under a 4.7% $\text{H}_2\text{-N}_2$ flow –in order to



avoid UO_2 oxidation— was conducted on all the green pellets. All disks were then calcined in three stages (100, 300 and 500°C) at $10^\circ\text{C}\cdot\text{min}^{-1}$ and held up to 4 hours to remove the incorporated EBS, followed by the sintering process at 1675°C for 4 hours ($5^\circ\text{C}\cdot\text{min}^{-1}$). Finally, polishing and thermal annealing were carried out to reveal grains (10 minutes at 1590°C under a 4.7% $\text{H}_2\text{-N}_2$ atmosphere). This fabrication process has been previously tested in our laboratory (Figure 5) [40].

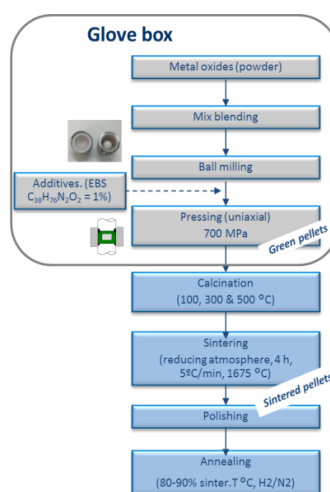


Figure 5 Fabrication flow diagram of conventional “dry route” used in CIEMAT for pellet production.

Green pellets were calcined during 30 min at 300 and 500°C using a ramp of $10^\circ\text{C}\cdot\text{min}^{-1}$. Finally, sintering conditions such as heating rate and sintering time were varied for UO_2 doped with 600 ppm of Cr_2O_3 , as it is shown in Table IV.

Sample / Reference	Heating cycles	Sintering time (h)
A	1600°C ($5^\circ\text{C}\cdot\text{min}^{-1}$) + 1695°C ($1^\circ\text{C}\cdot\text{min}^{-1}$)	4
B	1695°C ($5^\circ\text{C}\cdot\text{min}^{-1}$)	
C	1600°C ($5^\circ\text{C}\cdot\text{min}^{-1}$) + 1695°C ($1^\circ\text{C}\cdot\text{min}^{-1}$)	6
D	1695°C ($5^\circ\text{C}\cdot\text{min}^{-1}$)	
E	1600°C ($5^\circ\text{C}\cdot\text{min}^{-1}$) + 1695°C ($1^\circ\text{C}\cdot\text{min}^{-1}$)	10
F	1695°C ($5^\circ\text{C}\cdot\text{min}^{-1}$)	

Table IV Heating stages and sintering time, include label for each system. UO_2 doped with 600 ppm Cr_2O_3 .



Ciemat DIVISIÓN DE FISIÓN NUCLEAR	INFORME DFN/RA-03/SP-24	HOJA 14 DE 38
	REF. EXTERNA	REVISIÓN 0 FECHA 12/04/2024

2.2. EFFECT OF DOPANT CONTENT. MATERIALS: SAMPLE PREPARATION AND CHARACTERIZATION

For the objective 2 (see section 1), the effect of dopant content, UO₂ and Cr₂O₃ powders were provided by ENUSA and Alfa Aesar, respectively. UO₂ was thermally annealed in a 4.7% H₂-N₂ atmosphere at 1100°C to attain stoichiometric UO_{2.00}. UO₂ was mixed with weighted amounts of Cr₂O₃, together with 1% of EBS (Ethyl Bis Stearamide, C₃₈H₇₆N₂O₂, supplied by Tokyo Chemical Industry) as binder and lubricant [41], using low-energy ball milling. The batches of mixed powders were then blended for 1 minute at 15 Hz in a mixer mill, and then were pelletized as in section 2.1, applying a pressure of 700 MPa. As a result, a series of Cr₂O₃-doped UO₂ solid solutions were obtained. An undoped UO₂ sample was also prepared following the same procedure. In this work, a set of chromia-doped UO₂ disks have been sintered with different Cr₂O₃ concentrations. Table V shows the samples fabricated by this pathway.

Labelled Material	Cr ₂ O ₃ added (ppm)
UO ₂	0
UO ₂ _200Cr ₂ O ₃	200
UO ₂ _600Cr ₂ O ₃	600
UO ₂ _1000Cr ₂ O ₃	1000
UO ₂ _6000Cr ₂ O ₃	6000

Table V Definition of samples.



Ciemat DIVISIÓN DE FISIÓN NUCLEAR	INFORME DFN/RA-03/SP-24 REF. EXTERNA	HOJA 15 DE 38
		REVISIÓN 0 FECHA 12/04/2024

3. RESULTS

3.1. EFFECT OF SINTERING CONDITIONS

XRD analysis (Figure 6) and Raman spectroscopy (Figure 7) showed the Cr₂O₃ completely dissolved in the UO₂. The diffractogram reflections match a structure with space group Fm3m, with code 03-065-0285 from ICDD (ICDD-00-006-0504 for Cr₂O₃). Raman spectroscopy revealed in all samples the characteristic bands of pure UO₂ (T_{2g} mode at 445 cm⁻¹, corresponding to the vibration of the U-O bond, and the band centred around 1140 cm⁻¹ attributed to the 2LO overtone) without any band corresponding to Cr₂O₃. These results again confirm the incorporation of Cr₂O₃ into the UO₂ matrix. Additionally, a new band around 540 cm⁻¹ can be observed, attributed to the vacancies formation as a consequence of the incorporation of trivalent elements into the UO₂ matrix[34].

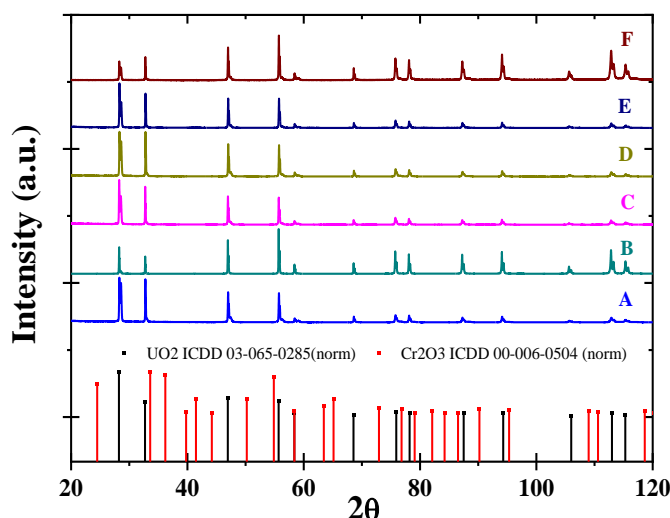


Figure 6 Diffraction patterns of doped UO₂ pellets with 600 ppm of Cr₂O₃ at different sintering conditions. See correspondence to labels in Table IV.



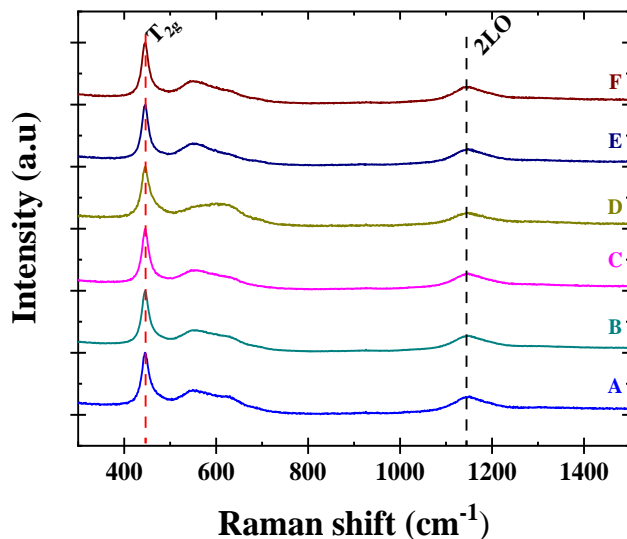


Figure 7 Raman spectra of doped UO_2 pellets with 600 ppm of Cr_2O_3 at different sintering conditions. See correspondence to labels in Table IV.

Figure 8 shows the grain size measured by the linear intercept method [42] from the images obtained by SEM (Figure 8.A) and the density measured by the Archimedean method by immersion in ethanol (Figure 8.B), where no noticeable variation in either of these two parameters is confirmed.

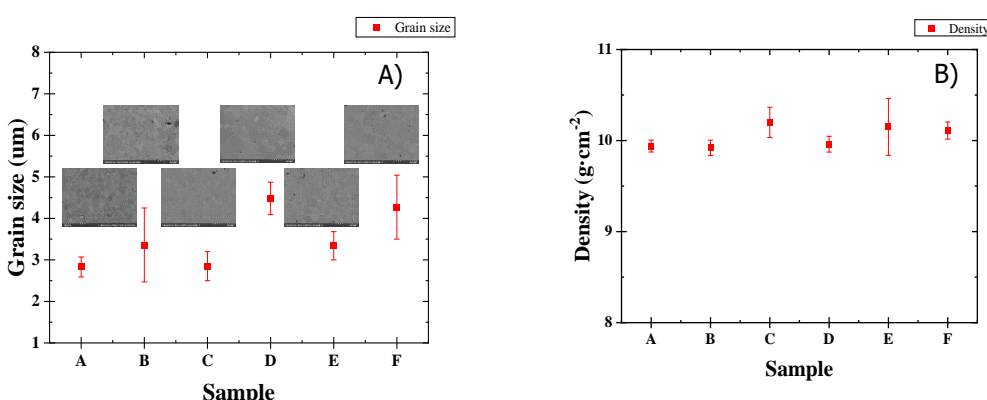


Figure 8 Grain size and SEM images (A) and density values (B). See correspondence to labels in ;Error! No se encuentra el origen de la referencia..



Figure 9.A shows the complete adsorption and desorption isotherms for surface area determination and porosimetry analysis. All samples reach maximum sorption at a relatively low pressure (P/P_0) range (0.20-0.60) is observed.

The specific surface area calculated by the standard BET method in N_2 [43] shows a clear trend (Figure 9.B). The lowest specific surface area values were obtained at longer sintering times (samples E and F). Within each sintering temperature, the value obtained with a ramp of $1^{\circ}C \cdot min^{-1}$ is lower than that achieved with a higher heating rate (Figure 9.B).

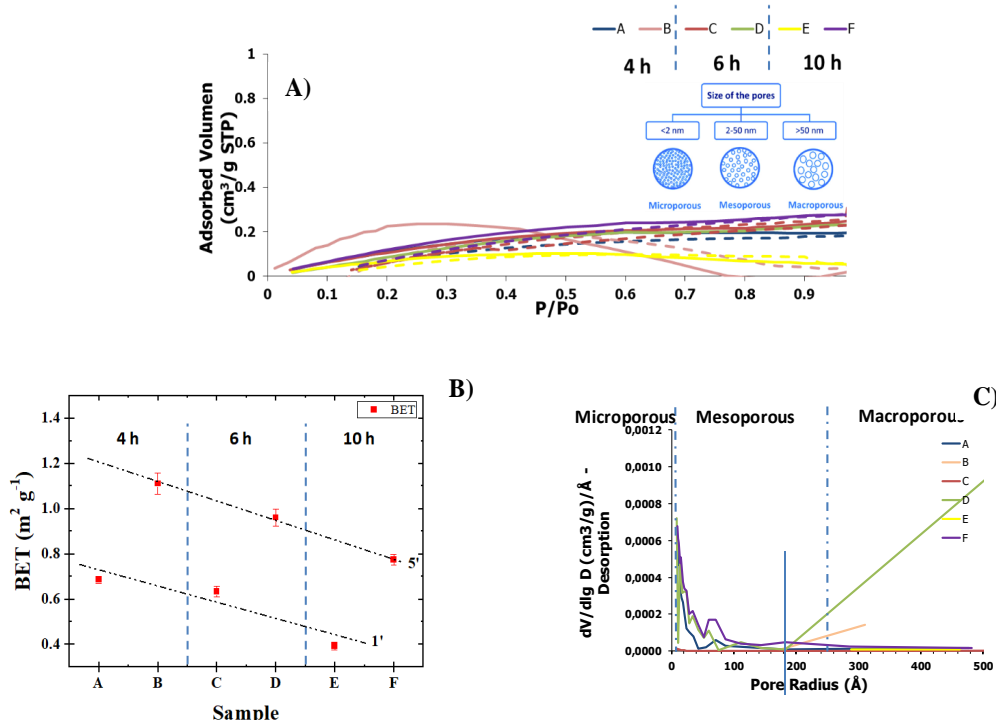


Figure 9 Adsorption isotherms (solid lines) and desorption isotherms (dashed lines) (A), BET surface area (B), and porosity analysis (C).

The desorption isotherm was used to determine the pore size distribution using the BJH method [43], where none of the samples exhibit microporosity as can be observed, with adsorption starting at pore sizes greater than 10 \AA . All the analysed samples have pore sizes below 100 \AA (mesopores).

Thus, no significant changes have been detected in the microstructural properties of UO_2 - $600Cr_2O_3$ pellets when changing the sintering times and heating rates (between 4 and 10 hours of heating and ramps of 1 and $5^{\circ}C \cdot min^{-1}$). The analysis of the fuel's pore size and



Ciemat DIVISIÓN DE FISIÓN NUCLEAR	INFORME DFN/RA-03/SP-24	HOJA 18 DE 38
	REF. EXTERNA	REVISIÓN 0 FECHA 12/04/2024

surface area confirms the absence of micropores in the fuel matrix, with porosity mostly associated to the mesopore range, typically observed in ceramic nuclear fuel matrices.

3.2. EFFECT OF DOPANT CONTENT

In the next sections, the effect of chromia on the sintered pellets will be studied by using the aforementioned techniques.

3.2.1. SEM: grain size and segregated phases

In the analyzed samples, grain size has been measured by taking SEM images and then using the linear intercept method [42, 44]. Representative images used for the calculation are shown in Figure 10, where an increase in the grain size can be seen when increasing Cr_2O_3 concentration and compared to pure UO_2 . Quantitative results of the average grain size in the doped pellets studied in this work are plotted in Figure 11.

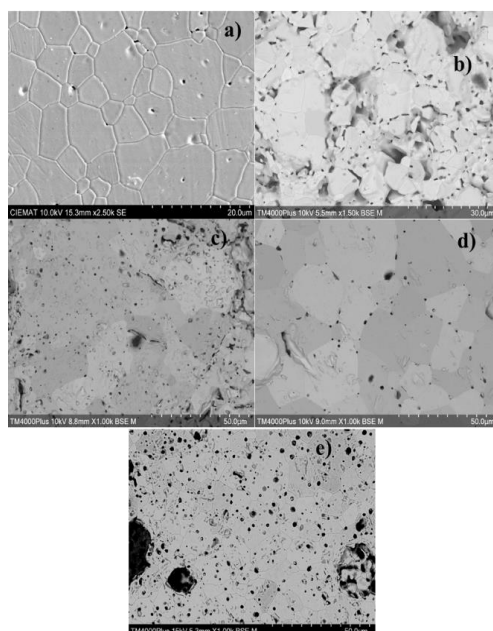


Figure 10 Representative SEM images of the analyzed pellets: a) pure UO_2 , b) $\text{UO}_2\text{-}200\text{Cr}_2\text{O}_3$, c) $\text{UO}_2\text{-}600\text{Cr}_2\text{O}_3$, d) $\text{UO}_2\text{-}1000\text{Cr}_2\text{O}_3$, e) $\text{UO}_2\text{-}6000\text{Cr}_2\text{O}_3$.

The distribution of the results shown in Figure 11 is analogous to grain size curves obtained in the same kind of fuels [13], but varying the absolute values, which depend on the specific sintering and annealing conditions (primarily heat treatment cycles: heating rates, holding



Ciemat DIVISIÓN DE FISIÓN NUCLEAR	INFORME DFN/RA-03/SP-24	HOJA 19 DE 38
	REF. EXTERNA	REVISIÓN 0 FECHA 12/04/2024

time and temperature). Grains of undoped UO₂ (0 ppm of Cr₂O₃ added) have the same average grain size that the Cr-doped sample with the lowest amount of dopant (200 ppm). These similar values suggest that a significant concentration of dopant is needed to appreciate the effects on the grain growth. When increasing Cr₂O₃ concentration, grain sizes are higher, reaching a maximum when 1000 ppm of Cr₂O₃ are added. With even higher values of dopant, average grain size decreases (Figure 11), thus demonstrating that the solubility limit has been reached and no more chromium enters into the UO₂ matrix. Beyond this solubility limit, excess dopant remains as inclusions in the grain boundaries, as proposed by Bourgeois et al. [13]. The presence of such precipitates inhibits the growth of the grains, *i.e.* the maximum grain size is obtained when the solubility limit of Cr³⁺ in UO₂ is reached (Figure 12).

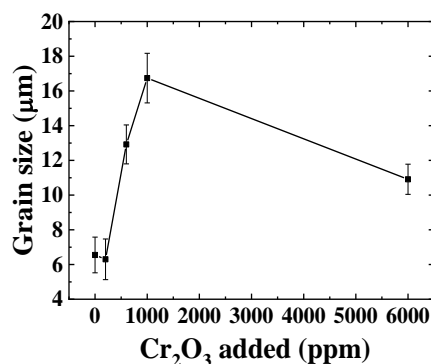


Figure 11 Average grain size of the studied disks vs Cr₂O₃ content. Uncertainty bands correspond to the repeatability of the measurements.

For each sintered disk, SEM images have been taken covering the major part of the surfaces, looking for segregated phases on the pellet. More and bigger precipitates were observed in the samples with a higher Cr₂O₃ content, especially in the sample with the highest concentration, 6000 ppm. This fact is expected taking into account that, in samples doped with 6000 ppm Cr₂O₃, chromium is beyond the solubility limit in the UO₂ matrix. However, even though in the other samples the solubility limit has not been reached yet, several small precipitates are still observed. This could be a result of the slow incorporation kinetics of Cr into the UO₂ matrix, and therefore the precipitates could be associated to the remnant of the initial powder particles, that are not dissolved [8].



Two images of representative Cr_2O_3 precipitates are shown in Figure 12. As can be seen (Figure 12a), the morphology of the precipitate, its size and the fact that it appears in the grain boundary could lead us to propose a chromium segregation, according to Yang et al. [45] and Bourgeois et al. [13]. Increasing the Cr_2O_3 concentration and exceeding the solubility limit, sample doped with 6000 ppm, the amount precipitated is much bigger, although it still appears in grain boundaries, as expected (Figure 12b).

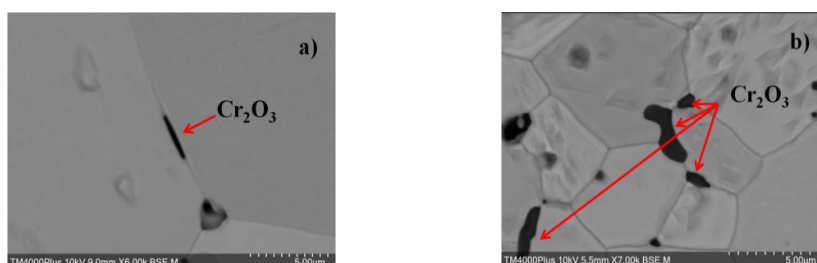


Figure 12 Back scattered SEM images of chromium precipitates in a grain boundaries in samples doped with a) 1000 ppm and b) 6000 ppm of Cr_2O_3 , respectively.

3.2.2. XRD

In order to study the lattice parameter evolution of the UO_2 pellets due to the presence of chromia, XRD was used and the corresponding diffractograms were obtained (Figure 13). It is known that the crystal structure of UO_2 is cubic, fluorite-type, so the lattice is characterized by only one lattice parameter (a). Diffraction peaks of all prepared samples were acquired under the same conditions, and a value for the lattice parameters was obtained from each one by using the unit cell refinement method, applying the corresponding error corrections. They are plotted in Figure 14.

From the diffraction peaks of each sample (Figure 13a), it can be seen that there is a shift to higher 2θ values with increasing Cr_2O_3 concentration. This effect is clearly observed in the 113° doublet (Figure 13b), indicating that the lattice parameter of the doped sample is smaller than that of undoped UO_2 , and the higher the concentration of dopant is, the lower lattice parameter value. This fact supports the densification of the samples. This lattice contraction as a consequence of introduction of chromium into the cubic UO_2 lattice is consistent with XRD results from Cardinaels et al. [16].



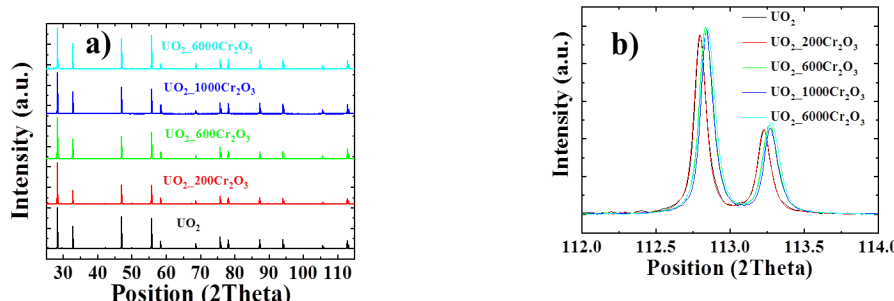


Figure 13 a) Diffraction patterns of the studied samples and b) the (531) $\text{K}\alpha_{1,2}$ doublet at 113° of the normalized diffraction patterns.

Código seguro de Verificación: GEN-5b4e-e946-617b-c6b0-3d9f-f9e9-eee5-61f3 | Puede verificar la integridad de este documento en la siguiente dirección:
<https://sara.ciemat.es:8443/csv/CsvRecoverService?csv=5b4ee946617bc6b03d9ff9e9eee561f3...>

To clearly visualize this lattice contraction as a function of chromium concentration, in Figure 14 the lattice parameter of the fabricated pellets versus the chromium mixed with the UO_2 in the monoliths fabrication is plotted. It can be seen that lattice parameter decreases linearly as a function of the chromia concentration until the solubility limit is reached. Nevertheless, the sample doped with 6000 ppm of Cr_2O_3 does not follow the same trend, due to the dissolution of the Cr^{3+} into the matrix reached the solubility limit under the conditions used in the fabrication of the pellet in this work, which according to the sintering conditions was established around 1000 ppm of Cr_2O_3 [8, 16].

In the selected range, the decrease in the lattice parameter follows a linear trend according to equation 1 in a good agreement with Vegard's law, which states that the lattice parameter of solid solutions vary linearly with the composition [46].

$$a(\text{nm}) = -1.92(\pm 0.25) \cdot 10^{-7}[\text{Cr}_2\text{O}_3](\text{ppm}) + 0.54724(\pm 0.00002) \quad (1)$$

The Vegard's law-like behavior when doping UO_2 with chromia has been also found by other authors [8, 16]. The contraction of the cubic lattice of UO_2 can be explained taking into account the defects that are created with the incorporation of a Cr^{3+} ion. When a U^{4+} ion is substituted by a Cr^{3+} ion, defect clusters are formed in order to maintain electroneutrality within the structure [13, 16]. The charge defect introduced in the lattice can be neutralized whether with the oxidation to U^{5+} by a nearby uranium atom, or by introducing oxygen vacancies. The net result of both effects is a contraction in the lattice parameter [16], specially taking into account that the ionic radius of Cr^{3+} is much smaller than that of U^{4+} (61 and 114 pm, respectively [47]). This has been confirmed by Cardinaels et al. [16], by using interatomic potentials calculations.



Ciemat DIVISIÓN DE FISIÓN NUCLEAR	INFORME DFN/RA-03/SP-24	HOJA 22 DE 38
REF. EXTERNA	REVISIÓN 0 FECHA 12/04/2024	

Although the Vegard's law-like behavior has been confirmed, it is valid only in the region where a complete solid solution is established [48]. This means that, from the data obtained by XRD, it is possible to deduce a solubility limit of Cr in the UO₂ matrix in these conditions. Assuming that beyond the solubility limit the lattice parameter will not further decrease, from the intersection of the Vegard's line and the horizontal line starting at the point of 6000 ppm of Cr₂O₃, this limit can be deduced; this calculation is rendered in Figure 14 (red square). This method has been validated to estimate solubility limits in other systems, such as Nb-doped UO₂ [49]. For the precise mathematical calculation, it has been obtained a solubility limit of (1094±23) ppm of Cr₂O₃, which corresponds to (748±16) ppm of Cr³⁺. This value is in good agreement with other studies carried out under similar sintering conditions, as reported by Leenaers et al. (860±30 ppm of Cr³⁺ [8]) and Bourgeois et al. (750 ppm of Cr³⁺ [13]). In addition, this limit supports the grain size behavior described in the previous section, as the highest grain size is found in the sample closest to the solubility limit.

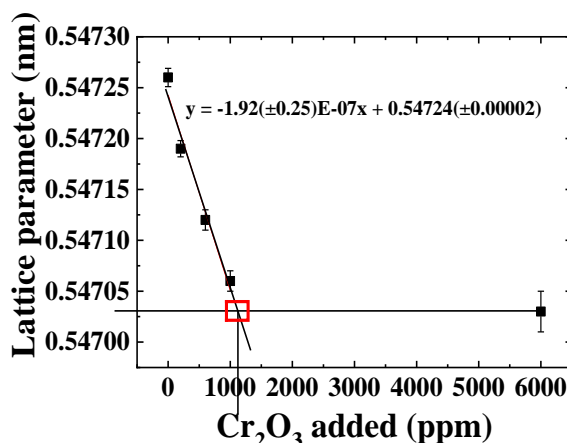


Figure 14 Lattice parameter vs Cr₂O₃ concentration and graphical calculation of solubility limit of Cr₂O₃ in the UO₂ matrix for the samples studied. Uncertainty bands correspond to the repeatability of the measurements.

Figure 15 shows a comparison between calculated lattice parameters and the grain size measurements of the chromia-doped UO₂ pellets. It should be highlighted that the maximum grain size is not reached with the lowest lattice parameter value. This is an indicator of the grain growth inhibition by the formation of precipitates in grain boundaries



[13], a process that not always occur when solubility limit has been reached (for example due to the slow incorporation kinetics of chromium [8]). In fact, this lattice parameter is reached when doping with a Cr_2O_3 concentration far beyond the solubility limit (6000 ppm), but in this case, the presence of chromia in grain boundary is so high that the average grain size is even lower than pellets doped with 600 ppm of Cr_2O_3 . The same reason of low incorporation kinetics of Cr^{3+} could also explain the behavior of the point labelled as $\text{UO}_2\text{-}200\text{Cr}_2\text{O}_3$ in Figure 15, which does not follow the linear trend of the grain size values, indicating that a minimum chromium amount may be necessary to promote the enlargement of pellet grains.

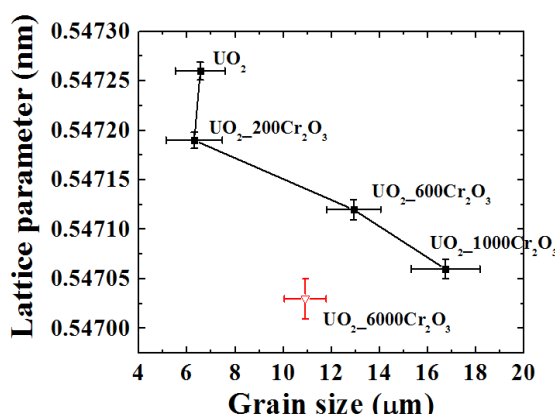


Figure 15 Lattice parameter vs average grain size of the analysed pellets. Black squares correspond to samples with Cr_2O_3 content lower than the solubility limit, while the open triangle represents the pellet doped with 6000 ppm of Cr_2O_3 , which is higher than the solubility limit. Uncertainty bands correspond to the repeatability of the measurements.

3.2.3. Raman spectroscopy and fluorescence spectral analysis

Figure 16 shows Raman spectra acquired from the UO_2 and chromia-doped UO_2 pellets. The plot represents the averaged spectra from 10 individual spectrums recorded at different locations of each disk.



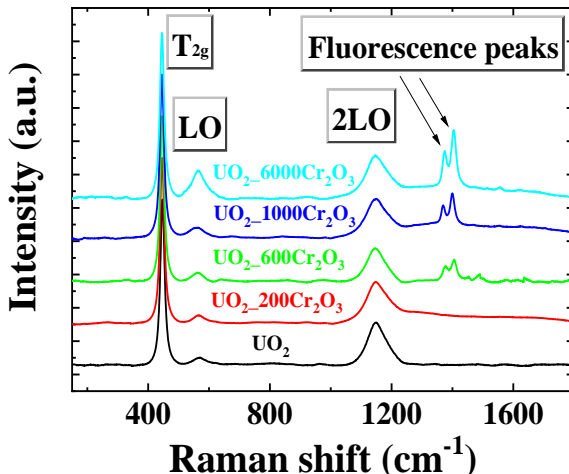


Figure 16 Raman spectra of chromia-doped UO_2 pellets.

The known Raman features of an undistorted, face-centered cubic structure like undoped UO_2 [50, 51] are seen at Figure 16. The same assignment that the one shown with powders (Table III entries a-c) is used here: T_{2g} mode at 445 cm^{-1} , the LO phonon at 570 cm^{-1} and the first overtone (2LO) at 1140 cm^{-1} . In addition, in some of the Raman spectra acquired from the doped pellets of this study, an extra feature to the previously described has been found. An intense doublet at around 1380 cm^{-1} and 1410 cm^{-1} (Figure 16) is observed and has been associated with fluorescence of Cr_2O_3 by several authors [37, 52-54].

3.2.3.1. Fluorescence

The presence of the formerly described fluorescence peaks is a consequence of a Cr_2O_3 -enriched region where the Raman laser spot has acquired the spectrum, thus there is chromium present at the surface of the pellet and has not entered in the UO_2 matrix. This hypothesis suggests that the higher Cr_2O_3 precipitates in the pellet-surface, the higher probability of finding fluorescence peaks in the Raman spectra, which are acquired 10 times per pellet randomly along the surface. Despite this reduced statistical sampling, the frequency histogram shown in Figure 17 confirms this hypothesis. This finding supports the behavior of Cr_2O_3 previously revealed in the SEM section, as more peaks assigned to the fluorescence of Cr^{3+} are found in the sample that presents more Cr_2O_3 precipitates, *i.e.* $\text{UO}_2\text{-}6000\text{Cr}_2\text{O}_3$.



Ciemat DIVISIÓN DE FISIÓN NUCLEAR	INFORME DFN/RA-03/SP-24	HOJA 25 DE 38
REF. EXTERNA	REVISIÓN 0 FECHA 12/04/2024	

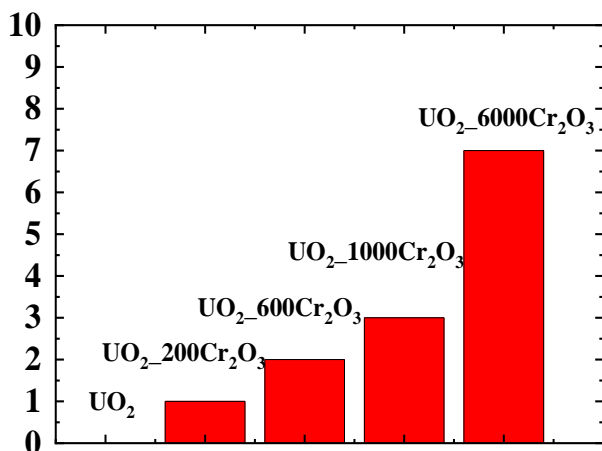


Figure 17 Number of spectrums showing Cr³⁺-fluorescence peaks (per 10 spectrums acquired for each simple).

3.2.3.2. Raman Intensity

On the one hand, T_{2g} and 2LO modes have been analyzed in terms of their intensities.

The T_{2g} mode involves the U-O bond stretching, and 2LO is attributed to a crystal electric field transition. This latter band has been proposed as a fingerprint for a quasi-perfect fluorite lattice [55, 56]. The observed intensity of the Raman scattered radiation depends, among other factors, on the instrumental and configuration parameters such as laser power or wavelength, optical path variations, sample placement acquisition and accumulation time, etc. Here all these instrumental parameters have been kept constant to perform a comparison of the absolute intensity, which is related to the Raman cross-section. Figure 18 shows the changes in absolute areas, i.e. integrated intensity, of the two mentioned bands. A marked decrease is observed when increasing Cr₂O₃ concentration, due to the distortions introduced in the lattice as a result of the entry of the doping agent. The fact that this area decrease is found in both peaks (445 and 1140 cm⁻¹) may indicate the unlikelihood that they can be attributed to variations in surface roughness.



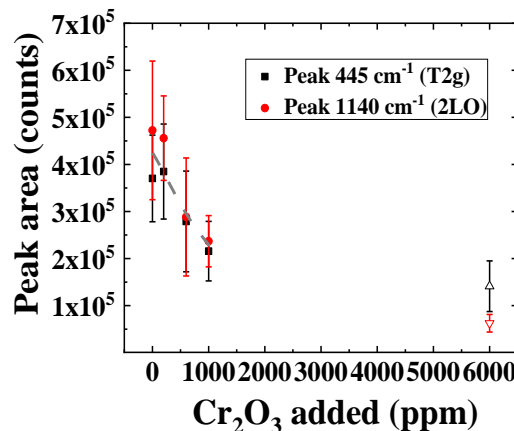


Figure 18 Area evolution of the T_{2g} (445 cm⁻¹) and 2LO (1140 cm⁻¹) bands with Cr₂O₃ concentration. Solid symbols correspond to samples with Cr₂O₃ content lower than the solubility limit, while open triangles represent the pellet doped with 6000 ppm of Cr₂O₃, which is higher than the solubility limit. Dashed line represents a guide to the eye to show the general trend of data. Uncertainty bands correspond to the repeatability of the measurements.

3.2.3.3. Profile Analysis of the LO Band

On the other hand, the band at 570 cm⁻¹ was analyzed in detail. A profile analysis was performed by obtaining the second derivative of the spectra. This examination revealed the contribution of two Lorentzian peaks, which indicates the presence of an additional feature band centered at 545 cm⁻¹ that was not observed in pure UO₂ spectra. This new feature and a more detailed study can be observed in Figure 19.



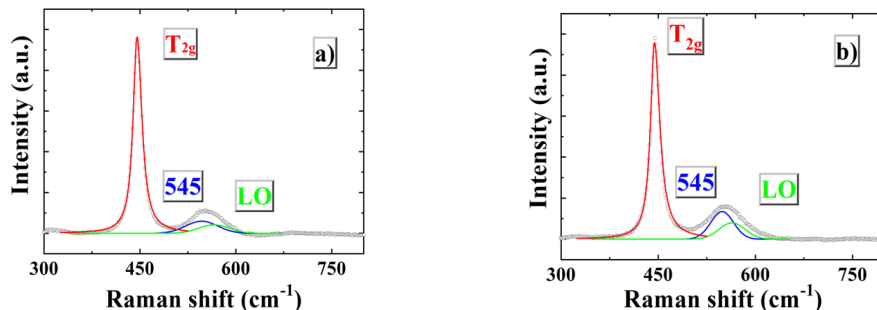


Figure 19 Raman spectra of a UO_2 disk doped with a) 600 ppm and b) 1000 ppm of Cr_2O_3 by Lorentzian peaks at 445, 545 and 570 cm^{-1} .

In Figure 19, the LO mode at 570 cm^{-1} increases in intensity with chromia content, together with the band at 545 cm^{-1} . This latter band is not observed for pure UO_2 , and it has been related to the creation of oxygen vacancies in other trivalent-doped UO_2 fuels systems, such as Gd and Dy [57], Nd [58], or La [59]; thus same assignment can be made when doping with Cr^{3+} . This is a result of the charge imbalance produced by the introduction of the trivalent dopant (substitution of a U^{4+} for a Cr^{3+}), and therefore produces a lattice distortion, as confirmed by XRD (see section 3.2). In addition, the assignment of this feature to the presence of oxygen vacancies can be confirmed by comparing with the Raman spectroscopic studies performed by Rao et al. [60] with $\text{ThO}_2\text{-UO}_2$ solid solutions, who did not report the presence of this band from the analysis of Th^{4+} doped UO_2 . In fact, the substitution of U^{4+} by Th^{4+} does not produce a charge imbalance and therefore no oxygen vacancies are created. It is important to highlight that this new band centered around 545 cm^{-1} has been observed only when Cr_2O_3 nominal concentration was beyond 600 ppm (Figure 20).

The band at 570 cm^{-1} has been ascribed to a first-order LO phonon [32]. Its observation has been related to lattice distortions, causing a breakdown in the selection rules [33], and allowing the appearance of this forbidden Raman scattering mode. As in the previous case, similar bands have been observed in other systems, such as hyper-stoichiometric UO_{2+x} [33] and for another kind of doped UO_2 materials [58, 59].

The calculated area of these features and the area ratio relative to that of the T_{2g} band have been plotted against the Cr_2O_3 concentration added at the beginning of the sintering process.



This plot can be seen in Figure 20. This calculated ratio emphasizes the dependence of the oxygen vacancies in the matrix structure with increasing chromia content.

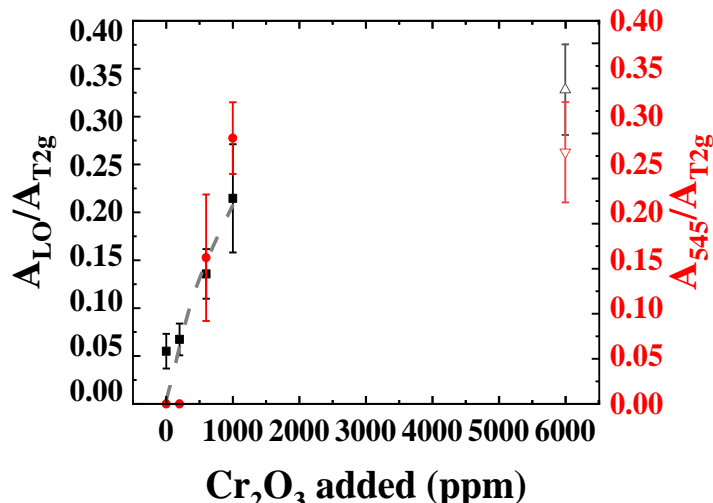


Figure 20 Evolution of the intensity of the peaks at 570 cm⁻¹ (LO band, black squares) and 545 cm⁻¹ (red circles), both referred to the T_{2g} band, with the Cr₂O₃ content. Solid symbols correspond to samples with Cr₂O₃ content lower than the solubility limit, while open triangles represent the pellet doped with 6000 ppm of Cr₂O₃, which is higher than the solubility limit. Dashed line represents a guide to the eye to show the general trend of data. Uncertainty bands correspond to the repeatability of the measurements.

Código seguro de Verificación: GEN-5b4e-e946-617b-c6b0-3d9f-f9e9-eee5-61f3 | Puede verificar la integridad de este documento en la siguiente dirección:
<https://sara.ciemat.es:8443/csv/CsvRecoverService?csv=5b4ee946617bc6b03d9ff...>

When detected, both the 545 and 570 cm⁻¹ area ratios are in the same range, and both undergo the same increase with dopant concentration. These evidences strongly support the assumption that both features are related to the dissolution of Cr³⁺ in the UO₂ solid matrix and then, to defects in the fluorite lattice induced by oxygen vacancies. Some authors have reported an additional band at 620–630 cm⁻¹ associated with the presence of cuboctahedral clusters of the oxidized phase U₄O₉, both in UO₂ and rare-earth doped samples [61–63]. The lack of this band in our spectra testifies that this phase has not been formed on the surfaces of the samples studied in this work, due to the final preparation performed to the pellets during the sintering process (thermal treatment under reducing atmosphere; 4.7% H₂-N₂). In addition, it also confirms that no self-oxidation of the sample by laser heating during the measurements has occurred.



As done before for the XRD results (Figure 15), the area ratio of this band has been compared with the average grain size values of the samples obtained by SEM (Figure 21). Again, maximum grain size is not reached with maximum A_{LO}/A_{T2g} , due to the segregation in the grain boundaries of the Cr_2O_3 that has not been incorporated in the UO_2 matrix [8, 13]. It should be highlighted that uncertainty intervals for samples UO_2 and $UO_2\text{-}200Cr_2O_3$ overlap, supporting that a minimum amount of Cr may be needed to promote grain enlargement.

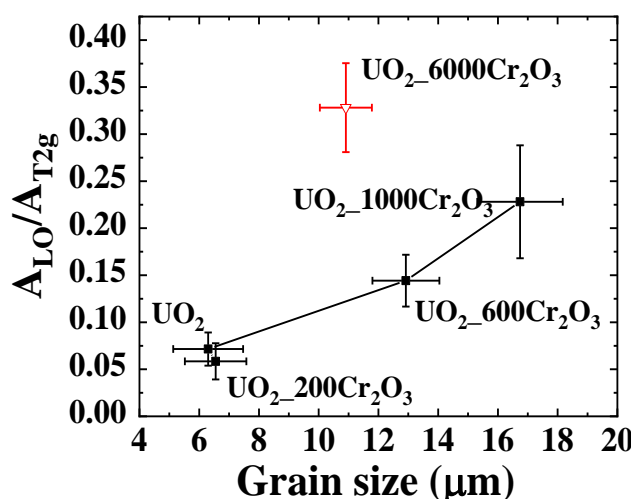


Figure 21 LO band area ratio vs grain size of the analysed pellets. Black squares correspond to samples with Cr_2O_3 content lower than the solubility limit, while the open triangle represents the pellet doped with 6000 ppm of Cr_2O_3 , which is higher than the solubility limit. Uncertainty bands correspond to the repeatability of the measurements.

Finally, from the combination of both XRD and Raman spectroscopy, one can extract interesting data that may help to understand the dissolution of Cr^{3+} into the UO_2 matrix. In Figure 22, a plot of the lattice parameter obtained by XRD versus the area ratio of the LO band (570 cm^{-1}) relative to the T_{2g} mode (445 cm^{-1}) obtained by Raman is presented. The tendency shown by the points indicates stabilization around values close to the calculated solubility limit, approximately near the labelled point $UO_2\text{-}1000Cr_2O_3$, as the decrease in lattice parameter values and the increase in the area ratio are not so marked. The quasi-linear behavior between the lattice parameter and the area ratio is a further key indicator of the



validity of Raman spectroscopy to analyze Cr-doped UO₂ pellets, since the correspondence with a well-established technique such as XRD is almost total.

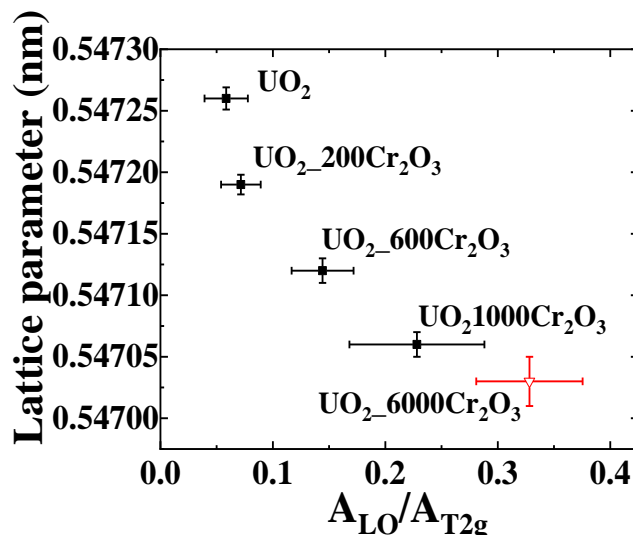


Figure 22 Lattice parameter vs A_{LO}/A_{T2g} peaks ratio. Black squares correspond to samples with Cr₂O₃ content lower than the solubility limit, while the open triangle represents the pellet doped with 6000 ppm of Cr₂O₃, which is higher than the solubility limit. Uncertainty bands correspond to the repeatability of the measurement.



Ciemat DIVISIÓN DE FISIÓN NUCLEAR	INFORME DFN/RA-03/SP-24	HOJA 31 DE 38
	REF. EXTERNA	REVISIÓN 0 FECHA 12/04/2024

4. CONCLUSIONS

Firstly, ATF pellets have been produced through a conventional metallurgical process, successfully incorporating the Cr dopant into the UO₂ matrix structure.

On the one hand, the influence of sintering conditions (heating rates, times, and sintering temperatures) has been tested on UO₂ matrix doped with Cr₂O₃. This analysis has been carried out by studying relevant physical parameters for fuel characterization, such as grain size, porosity, specific surface area, and density. All the tests conducted indicate that a sintering time of 4 hours achieves the optimal microstructural properties without energy consuming (currently a key factor, both economically and environmentally). No significant changes have been observed in the microstructural properties of the fuel pellets when varying the sintering times and heating rates (between 4 and 10 hours of heating and ramps of 1 and 5°C·min⁻¹). The analysis of the fuel's pore size and surface area, key factors for subsequent safety and integrity studies, confirms the absence of micropores in the fuel matrix, with porosity mostly associated to the mesopore range, which is typically observed in ceramic nuclear fuel matrices. The effect of oxygen partial pressure and pressing pressures are still expected to be done. The application of new processes and methods in ATF fabrication is in progress to understand the fuel response in different environments as a function of the precursor's nature and manufacture procedure.

On the other hand, Raman spectroscopy has been used to characterize Cr-doped UO₂ pellets with different chromia contents. The variation of the Raman modes with Cr₂O₃ concentration is studied and related to the creation of oxygen vacancies due to the entry of Cr³⁺ in the UO₂ matrix. The study of the grain size of the doped samples sintered at the same conditions reveals that the highest value is found for the sample with the amount of Cr₂O₃ closest to the solubility limit. This is interpreted in terms of the restriction of the grain growth by the presence of segregated phases. SEM images have shown that precipitates of Cr₂O₃ are found to be in the grain boundaries, and that more and bigger precipitates are found for the sample UO₂_6000Cr₂O₃. However, Cr₂O₃-rich areas in the surface of the pellets are also found in samples where the solubility limit has not been reached, probably due to the low incorporation kinetics of Cr. Its presence is supported by the appearance of their characteristic fluorescence peaks in several Raman spectra. Therefore, the quantity of doping agent and/or fabrication methods for real fuel must be optimized. By XRD, the solubility



Ciemat DIVISIÓN DE FISIÓN NUCLEAR	INFORME DFN/RA-03/SP-24	HOJA 32 DE 38
	REF. EXTERNA	REVISIÓN 0 FECHA 12/04/2024

limit of Cr in these specific sintering conditions is estimated to be (748±16) ppm. In summary, a systematic measurement protocol by Raman spectroscopy has been successfully developed to characterize Cr-doped UO₂ fuels.

These results could be valuable to be transferred to interested end users in Spain with which we have a professional relationship like ENRESA agency and/or ENUSA (nuclear fuel supplier).

Código seguro de Verificación: GEN-5b4e-e946-617b-c6b0-3d9f-f9e9-eee5-61f3 | Puede verificar la integridad de este documento en la siguiente dirección:
<https://sara.ciemat.es:8443/csv/CsvRecoverService?csv=5b4ee946617bc6b03d9ff9e9eee561f3...>

CSV : GEN-5b4e-e946-617b-c6b0-3d9f-f9e9-eee5-61f3

DIRECCIÓN DE VALIDACIÓN : <https://sara.ciemat.es:8443/csv/CsvRecoverService?csv=5b4ee946617bc6b03d9ff9e9eee561f3>

FIRMANTE(1) : M.SOLEDAD FERNANDEZ FERNANDEZ | FECHA : 28/05/2024 12:37 | Sin acción específica

FIRMANTE(2) : MARIA NIEVES RODRIGUEZ VILLAGRA | FECHA : 28/05/2024 12:38 | Sin acción específica

FIRMANTE(3) : SERGIO FERNANDEZ CARRETERO | FECHA : 28/05/2024 12:39 | Sin acción específica



Ciemat DIVISIÓN DE FISIÓN NUCLEAR	INFORME DFN/RA-03/SP-24	HOJA 33 DE 38
	REF. EXTERNA	REVISIÓN 0 FECHA 12/04/2024

5. ACKNOWLEDGEMENTS

This research is part of the project of R+D+i PID2021-124913OA-I00, IONMAT project funded by MICIU/AEI/10.13039/501100011033/, Proyectos de Generación de Conocimiento 2021. Authors also want to thank the funding for this research from the European Commission Horizon 2020 Research and Training Programme DisCo (Modern Spent Fuel Dissolution and Chemistry in Failed Container Conditions), under Grant Agreement No. 755443 and PATRICIA (Partitioning And Transmuter Research Initiative in a Collaborative Innovation Action), under Grant Agreement No. 945077.

Código seguro de Verificación: GEN-5b4e-e946-617b-c6b0-3d9f-f9e9-eee5-61f3 | Puede verificar la integridad de este documento en la siguiente dirección:
<https://sara.ciemat.es:8443/csv/CsvRecoverService?csv=5b4ee946617bc6b03d9ff9e9eee561f3...>

CSV : GEN-5b4e-e946-617b-c6b0-3d9f-f9e9-eee5-61f3

DIRECCIÓN DE VALIDACIÓN : <https://sara.ciemat.es:8443/csv/CsvRecoverService?csv=5b4ee946617bc6b03d9ff9e9eee561f3>

FIRMANTE(1) : M.SOLEDAD FERNANDEZ FERNANDEZ | FECHA : 28/05/2024 12:37 | Sin acción específica

FIRMANTE(2) : MARIA NIEVES RODRIGUEZ VILLAGRA | FECHA : 28/05/2024 12:38 | Sin acción específica

FIRMANTE(3) : SERGIO FERNANDEZ CARRETERO | FECHA : 28/05/2024 12:39 | Sin acción específica



Ciemat DIVISIÓN DE FISIÓN NUCLEAR	INFORME DFN/RA-03/SP-24	HOJA 34 DE 38
	REF. EXTERNA	REVISIÓN 0 FECHA 12/04/2024

6. REFERENCES

- [1] U.S. DOE, Roadmap: Development of Light Water Reactor Fuels with Enhanced Accident Tolerance. Report to Congress., (2015).
- [2] IAEA, Accident Tolerant Fuel Concepts For Light Water Reactors. Proceedings Of A Technical Meeting Held At Oak Ridge National Laboratories, United States Of America, 13–16 October 2014, (2016), IAEA-TECDOC-1797.
- [3] OECD-NEA, State-of-the-art Report on Innovative Fuels for Advanced Nuclear Systems, (2014), 6895.
- [4] OCDE/NEA, State-of-the-Art Report on Light Water Reactor Accident-Tolerant Fuels, (2018), 7317.
- [5] J. Arborelius, K. Backman, L. Hallstadius, M. Limbäck, J. Nilsson, B. Rebensdorff, G. Zhou, K. Kitano, R. Löfström, G. Rönnberg, Advanced Doped UO₂ Pellets in LWR Applications, Journal of Nuclear Science and Technology 43 (2006) 967-976.
- [6] K. Backman, L. Hallstadius, G. Roennberg, Westinghouse Advanced Doped Pellet - Characteristics and Irradiation Behaviour, (2010), (IAEA-TECDOC-1654).
- [7] Z. Guo, R. Ngayam-Happy, M. Krack, A. Pautz, Atomic-scale effects of chromium-doping on defect behaviour in uranium dioxide fuel, Journal of Nuclear Materials 488 (2017) 160-172.
- [8] A. Leenaers, L. de Tollenaere, C. Delafoy, S. Van den Berghe, On the solubility of chromium sesquioxide in uranium dioxide fuel, Journal of Nuclear Materials 317(1) (2003) 62-68.
- [9] E. Hellestrand, Burnable poison reactivity control and other techniques to increase fuel burnup in LWR fuel cycles, Trans. Am. Nucl. Soc. 40 (1982).
- [10] W. Böhm, H.D. Kiehlmann, A. Nuefert, M. Peehs, Gd₂O₃ up to 9 weight percent, an established burnable poison for advanced fuel management in pressurized water reactors, Kerntechnik (1987) 234.
- [11] K.A. Gamble, G. Pastore, D. Andersson, M. Cooper, ATF material model development and validation for priority fuel concepts, (2019), CASL-U-2019-1870-000.
- [12] C. Riglet-Martial, P. Martin, D. Testemale, C. Sabathier-Devals, G. Carlot, P. Matheron, X. Iltis, U. Pasquet, C. Valot, C. Delafoy, R. Largentot, Thermodynamics of chromium in UO₂ fuel: A solubility model, Journal of Nuclear Materials 447(1) (2014) 63-72.
- [13] L. Bourgeois, P. Dehaudt, C. Lemaignan, A. Hammou, Factors governing microstructure development of Cr₂O₃-doped UO₂ during sintering, Journal of Nuclear Materials 297(3) (2001) 313-326.



Ciemat DIVISIÓN DE FISIÓN NUCLEAR	INFORME DFN/RA-03/SP-24	HOJA 35 DE 38
	REF. EXTERNA	REVISIÓN 0 FECHA 12/04/2024

- [14] S. Kashibe, K. Une, Effect of additives (Cr₂O₃, Al₂O₃, SiO₂, MgO) on diffusional release of ¹³³Xe from UO₂ fuels, Journal of Nuclear Materials 254(2) (1998) 234-242.
- [15] I. Greenquist, M. Tonks, M. Cooper, D. Andersson, Y. Zhang, Grand potential sintering simulations of doped UO₂ accident-tolerant fuel concepts, Journal of Nuclear Materials 532 (2020) 152052.
- [16] T. Cardinaels, K. Govers, B. Vos, S. Van den Berghe, M. Verwerft, L. de Tollenaere, G. Maier, C. Delafoy, Chromia doped UO₂ fuel: Investigation of the lattice parameter, Journal of Nuclear Materials 424(1) (2012) 252-260.
- [17] T. Fujino, N. Sato, Analyses of the oxygen potential of the solid solutions M_yU_{1-y}O_{2+x} (M = M³⁺ and M²⁺) by statistics of defects and defect complexes, Journal of Nuclear Materials 189(1) (1992) 103-115.
- [18] H. Assmann, W. Dörr, G. Gradel, G. Maier, M. Peehs, Doping UO₂ with niobia — Beneficial or not?, Journal of Nuclear Materials 98(1) (1981) 216-220.
- [19] T. Yao, S.M. Scott, G. Xin, J. Lian, TiO₂ doped UO₂ fuels sintered by spark plasma sintering, Journal of Nuclear Materials 469 (2016) 251-261.
- [20] K. Une, M. Hirai, K. Nogita, T. Hosokawa, Y. Suzawa, S. Shimizu, Y. Etoh, Rim structure formation and high burnup fuel behavior of large-grained UO₂ fuels, Journal of Nuclear Materials 278(1) (2000) 54-63.
- [21] J. Arborelius, K. Backman, L. Hallstadius, M. Limback, J. Nilsson, B. Rebensdorff, G. Zhou, K. Kitano, R. Lofstrom, G. Ronnberg, Advanced Doped UO₂ Pellets in LWR Applications, Journal of Nuclear Science and Technology 43(9) (2006) 967-976.
- [22] IAEA, Advanced Fuel Pellet Materials and Fuel Rod Design for Water Cooled Reactors, INTERNATIONAL ATOMIC ENERGY AGENCY, Vienna, (2010).
- [23] S.M. Bragg-Sitton, M. Todosow, R. Montgomery, C.R. Stanek, R. Montgomery, W.J. Carmack, Metrics for the Technical Performance Evaluation of Light Water Reactor Accident-Tolerant Fuel, Nuclear Technology 195(2) (2016) 111-123.
- [24] A. Massih, Effects of additives on uranium dioxide fuel behavior, (2014), 2014:21.
- [25] J. Holm, Cr₂O₃ doped UO₂ fuel, BWR implementation. AREVA/NRC., 2015. <https://www.nrc.gov/docs/ml1518/ML15181A359.pdf>.
- [26] SNETP, Strategic Research And Innovation Agenda. Strategic research and innovation agenda (SRIA) . Brussels, Belgium, (2021).
- [27] S.F. N. Rodríguez-Villagra, A. Núñez, J.M. Elorrieta, A. Milena-Pérez, L. J. Bonales, L. Gutiérrez, L. Serrano, S. Durán, L. Anta, H. Galán, Innovación en tecnología de fabricación nuclear. Innovation Of Nuclear MAnufacturing Technology (IONMAT). (2023), DFN/RA-02/SP-23.



Ciemat DIVISIÓN DE FISIÓN NUCLEAR	INFORME DFN/RA-03/SP-24	HOJA 36 DE 38
	REF. EXTERNA	REVISIÓN 0 FECHA 12/04/2024

- [28] C. Madic, Overview of the hydrometallurgical and pyrometallurgical processes studied world-wide for the partitioning of high active nuclear wastes, NUCEF 2001, Japan, (2002).
- [29] J.N. Mathur, M.S. Murali, K.L. Nash, ACTINIDE PARTITIONING—A REVIEW, Solvent Extraction and Ion Exchange 19(3) (2001) 357-390.
- [30] S. Manna, R. Kumar, S.K. Satpati, S.B. Roy, J.B. Joshi, Study of the changes in composition of ammonium diuranate with progress of precipitation, and study of the properties of ammonium diuranate and its subsequent products produced from both uranyl nitrate and uranyl fluoride solutions, Nuclear Engineering and Technology 49(3) (2017) 541-548.
- [31] L.J. Bonales, N. Rodríguez-Villagra, I. Sánchez-García, O.R. Montoro, U(VI) speciation studies by Raman spectroscopy technique in the production of nuclear fuel, Progress in Nuclear Energy 145 (2022) 104122.
- [32] T. Livneh, E. Sterer, Effect of pressure on the resonant multiphonon Raman scattering in UO_2 , Physical Review B 73(8) (2006) 085118.
- [33] H. He, D. Shoesmith, Raman spectroscopic studies of defect structures and phase transition in hyper-stoichiometric UO_{2+x} , Physical Chemistry Chemical Physics 12(28) (2010) 8109-8118.
- [34] J.M. Elorrieta, L.J. Bonales, N. Rodriguez-Villagra, V.G. Baonza, J. Cobos, A detailed Raman and X-ray study of UO_{2+x} oxides and related structure transitions, Physical Chemistry Chemical Physics 18 (2016) 28209-28216.
- [35] M. Mohammadtaheri, Q. Yang, Y. Li, J. Corona-Gomez, The Effect of Deposition Parameters on the Structure and Mechanical Properties of Chromium Oxide Coatings Deposited by Reactive Magnetron Sputtering, Coatings 8(3) (2018) 111.
- [36] A.S.O. Gomes, N. Yaghini, A. Martinelli, E. Ahlberg, A micro-Raman spectroscopic study of $\text{Cr}(\text{OH})_3$ and Cr_2O_3 nanoparticles obtained by the hydrothermal method, Journal of Raman Spectroscopy 48(10) (2017) 1256-1263.
- [37] F. Adar, Raman Spectra of Metal Oxides, Spectroscopy 29(10) (2014) 14-22.
- [38] S.-H. Shim, T.S. Duffy, R. Jeanloz, C.-S. Yoo, V. Iota, Raman spectroscopy and x-ray diffraction of phase transitions in $\{\text{Cr}\}_{2}\{\text{O}\}_{3}$ to 61 GPa, Physical Review B 69(14) (2004) 144107.
- [39] Y. Ziouane, B. Arab-Chapelet, S. Lalleman, G. Leturcq, Effect of the Microstructural Morphology on UO_2 Powders, Procedia Chemistry 21 (2016) 319-325.
- [40] S. Fernandez, M.I. Nieto, J. Cobos, R. Moreno, CeO_2 pellet fabrication as spent fuel matrix analogue, Journal of the European Ceramic Society 36 (2016) 3505–3512.
- [41] J. Auborn, J. Choo, Mechanisms of lubrication in powder metallurgy, Advances in Powder Metallurgy and Particulate Materials (1993) 17-25.

Código seguro de Verificación : GEN-5b4e-e946-617b-c6b0-3d9f-f9e9-eee5-61f3 | Puede verificar la integridad de este documento en la siguiente dirección : <https://sara.ciemat.es:8443/csv/CsvRecoverService?csv=5b4ee946617bc6b03d9ff9e9eee561f3...>



Ciemat DIVISIÓN DE FISIÓN NUCLEAR	INFORME DFN/RA-03/SP-24	HOJA 37 DE 38
	REF. EXTERNA	REVISIÓN 0 FECHA 12/04/2024

- [42] ISO, ISO/FDIS 643:2012 "Steels-Micrographic determination of the apparent grain size", (2012).
- [43] E.P. Barrett, L.G. Joyner, P.P. Halenda, The Determination of Pore Volume and Area Distributions in Porous Substances. I. Computations from Nitrogen Isotherms, *Journal of the American Chemical Society* 73(1) (1951) 373-380.
- [44] K.W. Kang, J.H. Yang, J.H. Kim, Y.W. Rhee, D.J. Kim, K.S. Kim, K.W. Song, Improvement of UO₂ Pellet Properties by Controlling the Powder Morphology of Recycled U₃O₈ Powder, *Journal of Nuclear Science and Technology* 45(11) (2008) 1150-1154.
- [45] J.H. Yang, K.S. Kim, I.H. Nam, J.S. Oh, D.-J. Kim, Y.W. Rhee, J.H. Kim, Effect of step wise variation of oxygen potential during the isothermal sintering on the grain growth behavior in Cr₂O₃ doped UO₂ pellets, *Journal of Nuclear Materials* 429(1) (2012) 25-33.
- [46] L. Vegard, Die Konstitution der Mischkristalle und die Raumfüllung der Atome, *Zeitschrift für Physik* 5(1) (1921) 17-26.
- [47] R.D. Shannon, Revised effective ionic radii and systematic studies of interatomic distances in halides and chalcogenides, *Acta Crystallographica Section A* 32(5) (1976) 751-767.
- [48] M.M. Bućko, Ionic conductivity of CaO–Y₂O₃–ZrO₂ materials with constant oxygen vacancy concentration, *Journal of the European Ceramic Society* 24(6) (2004) 1305-1308.
- [49] Y. Harada, Sintering behaviour of niobia-doped large grain UO₂ pellet, *Journal of Nuclear Materials* 238(2) (1996) 237-243.
- [50] J.M. Elorrieta, L.J. Bonales, M. Naji, D. Manara, V.G. Baonza, J. Cobos, Laser-induced oxidation of UO₂: A Raman study, *Journal of Raman Spectroscopy* 49(5) (2018) 878-884.
- [51] P.G. Marlow, J.P. Russell, J.R. Hardy, Raman scattering in uranium dioxide, *The Philosophical Magazine: A Journal of Theoretical Experimental and Applied Physics* 14(128) (1966) 409-410.
- [52] J.J. Arnoux, G. Sutter, G. List, P. Bourson, H. Chaynes, Raman characterization of Ti–6Al–4V oxides and thermal history after kinetic friction, *Phase Transitions* 87(6) (2014) 559-570.
- [53] M.-F. Luo, P. Fang, M. He, Y.-L. Xie, In situ XRD, Raman, and TPR studies of CuO/Al₂O₃ catalysts for CO oxidation, *Journal of Molecular Catalysis A: Chemical* 239(1) (2005) 243-248.
- [54] S.E. Molis, D.R. Clarke, Measurement of Stresses Using Fluorescence in an Optical Microprobe: Stresses around Indentations in a Chromium-Doped Sapphire, *Journal of the American Ceramic Society* 73(11) (1990) 3189-3194.



Ciemat DIVISIÓN DE FISIÓN NUCLEAR	INFORME DFN/RA-03/SP-24	HOJA 38 DE 38
	REF. EXTERNA	REVISIÓN 0 FECHA 12/04/2024

- [55] N. Liu, J. Kim, J. Lee, Y.-S. Youn, J.-G. Kim, J.-Y. Kim, J.J. Noël, D.W. Shoesmith, Influence of Gd Doping on the Structure and Electrochemical Behavior of UO₂, *Electrochimica Acta* 247 (2017) 496-504.
- [56] D. Manara, B. Renker, Raman spectra of stoichiometric and hyperstoichiometric uranium dioxide, *Journal of Nuclear Materials* 321(2) (2003) 233-237.
- [57] M. Razdan, D.W. Shoesmith, Influence of Trivalent-Dopants on the Structural and Electrochemical Properties of Uranium Dioxide (UO₂), *Journal of The Electrochemical Society* 161(3) (2014) H105.
- [58] L. Desgranges, Y. Pontillon, P. Matheron, M. Marcket, P. Simon, G. Guimbretière, F. Porcher, Miscibility Gap in the U–Nd–O Phase Diagram: a New Approach of Nuclear Oxides in the Environment?, *Inorganic Chemistry* 51(17) (2012) 9147-9149.
- [59] Z. Talip, T. Wiss, P.E. Raison, J. Paillier, D. Manara, J. Somers, R.J.M. Konings, Raman and X-ray Studies of Uranium–Lanthanum-Mixed Oxides Before and After Air Oxidation, *Journal of the American Ceramic Society* 98(7) (2015) 2278-2285.
- [60] R. Rao, R.K. Bhagat, N.P. Salke, A. Kumar, Raman spectroscopic investigation of thorium dioxide-uranium dioxide (ThO₂-UO₂) fuel materials, *Appl Spectrosc* 68(1) (2014) 44-8.
- [61] J. Lee, J. Kim, Y.-S. Youn, N. Liu, J.-G. Kim, Y.-K. Ha, D.W. Shoesmith, J.-Y. Kim, Raman study on structure of U_{1-y}GdyO_{2-x} (y=0.005, 0.01, 0.03, 0.05 and 0.1) solid solutions, *Journal of Nuclear Materials* 486 (2017) 216-221.
- [62] J.K. Jeongmook Lee, Young-Sang Youn, Jong-Yun Kim and Sang Ho Lim, Surface characterization of (U,Nd)O₂: the influence of trivalent-dopant on structure of UO₂, *Progress in Nuclear Science and Technology* 5 (2018) 33-36.
- [63] L. Desgranges, G. Baldinozzi, P. Simon, G. Guimbretière, A. Canizares, Raman spectrum of U₄O₉: a new interpretation of damage lines in UO₂, *Journal of Raman Spectroscopy* 43(3) (2012) 455-458.

